The Astrophysical Journal, 830:141 (9pp), 2016 October 20 doi:10.3847/0004-637X/830/2/141

OBSERVED VARIABILITY AT 1 and 4 μm IN THE Y0 BROWN DWARF WISEP J173835.52+273258.9

S. K. Leggett[1], Michael C. Cushing[2], Kevin K. Hardegree-Ullman[2], Jesica L. Trucks[2], M. S. Marley[3], Caroline V. Morley[4], D. Saumon[5], S. J. Carey[6], J. J. Fortney[4], C. R. Gelino[7,8], J. E. Gizis[9], J. D. Kirkpatrick[7], and G. N. Mace[10]

[1] Gemini Observatory, Northern Operations Center, 670 N. A'ohoku Place, Hilo, HI 96720, USA; sleggett@gemini.edu
[2] The University of Toledo, 2801 West Bancroft Street, Mailstop 111, Toledo, OH 43606, USA
[3] NASA Ames Research Center, Mail Stop 245-3, Moffett Field, CA 94035, USA
[4] Department of Astronomy and Astrophysics, University of California, Santa Cruz, CA 95064, USA
[5] Los Alamos National Laboratory, P.O. Box 1663, MS F663, Los Alamos, NM 87545, USA
[6] Spitzer Science Center, CalTech, Pasadena, CA 91125, USA
[7] IPAC, CalTech, Pasadena, CA 91125, USA
[8] NASA Exoplanet Science Institute, CalTech, Pasadena, CA 91125, USA
[9] University of Delaware, Newark, DE 19716, USA
[10] University of Texas, Austin, TX 78712, USA

Received 2016 April 5; revised 2016 July 25; accepted 2016 July 26; published 2016 October 18

ABSTRACT

We have monitored photometrically the Y0 brown dwarf WISEP J173835.52+273258.9 (W1738) at both near- and mid-infrared wavelengths. This $\lesssim$1 Gyr old 400 K dwarf is at a distance of 8 pc and has a mass around 5 $M_{\rm Jupiter}$. We observed W1738 using two near-infrared filters at $\lambda \approx 1$ μm, *Y* and *J*, on Gemini Observatory and two mid-infrared filters at $\lambda \approx 4$ μm, [3.6] and [4.5], on the *Spitzer* observatory. Twenty-four hours were spent on the source by *Spitzer* on each of 2013 June 30 and October 30 UT. Between these observations, around 5 hr were spent on the source by Gemini on each of 2013 July 17 and August 23 UT. The mid-infrared light curves show significant evolution between the two observations separated by 4 months. We find that a double sinusoid can be fit to the [4.5] data, where one sinusoid has a period of 6.0 $\pm$ 0.1 hr and the other a period of 3.0 $\pm$ 0.1 hr. The near-infrared observations suggest variability with a ~3.0 hr period, although only at a $\lesssim 2\sigma$ confidence level. We interpret our results as showing that the Y dwarf has a 6.0 $\pm$ 0.1 hr rotation period, with one or more large-scale surface features being the source of variability. The peak-to-peak amplitude of the light curve at [4.5] is 3%. The amplitude of the near-infrared variability, if real, may be as high as 5%–30%. Intriguingly, this size of variability and the wavelength dependence can be reproduced by atmospheric models that include patchy KCl and Na_2S clouds and associated small changes in surface temperature. The small number of large features, as well as the timescale for evolution of the features, is very similar to what is seen in the atmospheres of the solar system gas giants.

Key words: brown dwarfs – stars: atmospheres – stars: individual (WISEP J173835.52+273258.9)

1. INTRODUCTION

There are now more than 20 brown dwarfs known in the solar neighborhood that have effective temperatures ($T_{\rm eff}$) lower than 500 K (Cushing et al. 2011, 2014; Luhman et al. 2011; Kirkpatrick et al. 2012; Liu et al. 2012; Tinney et al. 2012; Luhman 2014; Pinfield et al. 2014; Schneider et al. 2015). These have been classified as Y dwarfs (Cushing et al. 2011; Kirkpatrick et al. 2012). Evolutionary models show that for 300 K $\leqslant T_{\rm eff} \leqslant$ 500 K and 0.2 Gyr $\leqslant$ age $\leqslant$ 10 Gyr (as appropriate for the solar neighborhood) the mass range is 2–30 $M_{\rm Jupiter}$ (Saumon & Marley 2008). Hence, this population of isolated brown dwarfs has a mass that is very planet-like.

Our group has an ongoing program measuring the photometric variability of Y dwarfs. For warmer brown dwarfs variability is usually associated with inhomogeneous or variable cloud structure in the atmosphere (e.g., Radigan et al. 2012). For Y0 and Y1 dwarfs with $T_{\rm eff} \approx 400$ K the atmospheres are generally cloud-free, because most of the atmosphere is too cold for chloride or sulfide clouds and too warm for water or ammonia clouds (Burrows et al. 2003; Morley et al. 2012, 2014); in fact, cloud-free models can reproduce Y dwarf observations (Leggett et al. 2015, 2016). Nevertheless, variability may be seen at wavelengths where flux is emitted from very high and cold or low and warm layers, where condensates can be present (Morley et al. 2012), or variability may be seen due to temperature variations across the brown dwarf surface (Showman & Kaspi 2013).

In our first paper (Cushing et al. 2016, hereafter Cu16) we show that the Y0.5(pec) brown dwarf WISEPC J140518.40 +553421.5 (W1405; Cushing et al. 2011) is variable at mid-infrared wavelengths. W1405 was observed with *Spitzer* using the IRAC camera (Fazio et al. 2004) in the [3.6] and [4.5] filters. Variability was evident at [4.5] in the first epoch and at both [3.6] and [4.5] in the second epoch. The second-epoch light curves have a period of about 8.5 hr and semiamplitudes of 3.5%. In the current paper we present the detection of variability at mid-infrared wavelengths in another Y0, WISEP J173835.52+273258.9 (W1738; Cushing et al. 2011). We also present the tentative detection of variability at near-infrared wavelengths, at the $\lesssim 2\sigma$ confidence level. We extend to lower limits the work of Rajan et al. (2015), who excluded any *J*-band variability larger than 20% for this brown dwarf.

Leggett et al. (2016) compare near-infrared spectra and photometry for W1738 to recent models that include chemical disequilibrium driven by vertical transport (Tremblin et al. 2015). It was necessary to include mixing in order to reproduce the observations, and a cloud-free solar metallicity model with $T_{\rm eff} = 425 \pm 25$ K and log $g = 4.0 \pm 0.25$ fit the data best.

Table 1
Properties of WISEP J173835.52+273258.9

Property	Value	References
Spectral type	Y0	Cu11
Distance (pc)	7.8 ± 0.6	Be14
V_{tan} (km s^{-1})	17 ± 1	Be14
Rotation period (hr)	6.0 ± 0.1	This work
T_{eff} (K)	425 ± 25	Le16
log g (cm s^{-2})	4.0 ± 0.25	Le16
Mixing coefficient K_{zz} (cm^2 s^{-1})	10^6	Le16
Mass ($M_{Jupiter}$)	3–9	Le16
Age (Gyr)	0.15–1	Le16
Y_{MKO} (mag)	19.74 ± 0.08	This work
J_{MKO} (mag)	19.58 ± 0.04	This work
H_{MKO} (mag)	20.24 ± 0.08	Le16
K_{MKO} (mag)	20.58 ± 0.10	Le13
Ch.1(3.6 μm)$_{IRAC}$ (mag)	16.87 ± 0.03	Le13
Ch.2(4.5 μm)$_{IRAC}$ (mag)	14.42 ± 0.03	Le13
W1(3.4 μm)$_{WISE}$ (mag)	17.71 ± 0.16	AllWISE
W2(4.6 μm)$_{WISE}$ (mag)	14.50 ± 0.04	AllWISE
W3(12 μm)$_{WISE}$ (mag)	12.45 ± 0.40	AllWISE
Y variability semiamplitude (%)	5–15	This work, $\lesssim 2\sigma$ confidence
J variability semiamplitude (%)	3–8	This work, $\lesssim 2\sigma$ confidence
Ch.2(4.5 μm) variability semi-amplitude (%)	1.5	This work

Note. References: Beichman et al. (2014); Cushing et al. (2011); Leggett et al. (2013, 2016).

This temperature and relatively low gravity imply that W1738 is a 3–9 $M_{Jupiter}$ object with an age of 0.15–1 Gyr. Table 1 lists properties of W1738.

In Section 2 we present new observations of W1738 obtained with *Spitzer* IRAC and Gemini Observatory and its near-infrared imager NIRI (Hodapp et al. 2003). We obtained two epochs of [3.6] and [4.5] data, separated by 4 months, as well as two epochs of near-infrared Y and J data, obtained between the *Spitzer* observations and separated by 1 month. Section 3 presents our analysis of the data, which we discuss in Section 4. Our conclusions are given in Section 5.

2. OBSERVATIONS

2.1. Gemini NIRI Observations

W1738 was observed as part of the Gemini North program GN-2013A-Q-21. The brown dwarf was imaged in the Y and J filters using NIRI. The NIRI Y filter differs slightly from the MKO standard, where $Y_{NIRI} - Y_{MKO} = 0.17 \pm 0.03$ mag for late-type T and early-type Y dwarfs (Liu et al. 2012).

Long-duration observations were obtained on UT 2013 July 17 and August 23 in photometric conditions with typical seeing 0.″8. Integration times for both filters were 60 s, and offsets of about 12″ were used in dither patterns that were moved slightly on the detector through the observation, to minimize the impact of bad pixels and reduce any flat-fielding artifacts. The filters were alternated so that a five-position dither in Y was executed, followed by a nine-position dither in J, followed by another five-position dither in Y, etc.

On 2013 July 17 the observation ran from UT 07:22:57 to 12:18:09, for a duration of 4.92 hr. Seventeen five-position dithers in Y and 16 nine-position dithers in J were obtained, for an on-source time of 1.4 hr in Y and 2.4 hr in J. On 2013 August 23 the observation ran from UT 5:41:48 to 10:19:56, for a duration of 4.64 hr. Sixteen five-position dithers in Y and 15 nine-position dithers in J were obtained, for an on-source time of 1.3 hr in Y and 2.3 hr in J. Photometric standard FS 27 was observed before the W1738 observation, and FS 35 was observed after, on both nights. The data were reduced in the standard way, using dark and flat-field images, obtained with the on-telescope calibration unit, and Gemini IRAF routines.

The NIRI detector suffers from first-frame pattern noise, which occurs in the first frame following any filter change. Because of this, we discarded all of the first frames in each set and used sets of four Y images and sets of eight J images to first generate sky frames and then co-added images. Aperture photomery with annular skies and an aperture diameter of 2.″4 was performed.

Six stars (or point-like objects) with Y and J magnitudes between 17 and 18 provided the photometric baseline reference. We used five point sources with Y and J magnitudes between 18.9 and 20.7 to further explore the precision of the photometry, in order to determine whether or not the similarly bright W1738 is variable in these filters. The 11 sources were selected for brightness and for being present in every co-added image with a clean annular sky region. The uncertainty in the photometry obtained from the 4-minute Y and 8-minute J co-added images was 1%–2% for the brighter reference stars in both filters and ∼5% in Y and ∼3% in J for W1738 and the five fainter point sources. Figure 1 shows examples of a co-added 4-minute Y and 8-minute J image, with W1738 and the 11 other sources identified. Table 2 gives the nightly average of the photometry for W1738 and the other sources. The last two co-added images for each filter on the night of 2013 August 23 suffered from poor seeing, and while the data were used for relative photometry, the absolute values in Table 2 exclude these two data points.

We compared the photometry of W1738 and the five fainter sources to the six brighter reference stars, and we also compared each bright reference star to the other five reference stars as a check on data quality. Figures 2 and 3 show the resulting light curves for each night. These are discussed in Section 3.

2.2. Spitzer IRAC Observations

W1738 was observed in both the [3.6] and [4.5] filters of the IRAC camera on *Spitzer*, with the filters observed consecutively. For each filter 12.0 hr long observations were obtained, and the 24.0 hr long observation with the filter pair was repeated 4 months later. The first epoch ran from UT 2013 June 29 19:22:39.36 to 2013 June 30 07:23:48.48 for [3.6], and from 2013 June 30 07:30:00.00 to 19:31:26.40 for [4.5]. The second epoch ran from UT 2013 October 29 18:29:22.56 to 2013 October 30 06:30:31.68 for [3.6], and from 2013 October 30 06:36:25.92 to 18:37:52.32 for [4.5]. The data were obtained as part of program 90015 during campaigns 35100 and 35900. The data were obtained and reduced in the same way as that for W1405, as decribed in Cu16. Briefly, the 100 s images were obtained in "staring" mode for each filter. Photometric analysis starts with the basic calibrated data frames, which are converted from units of MJy sr^{-1} to electrons. Aperture photometry with a radius of 3 pixels and a background annulus is then obtained using a custom Interactive Data Language (IDL) code. For W1738 the field was more crowded than that of W1405, and

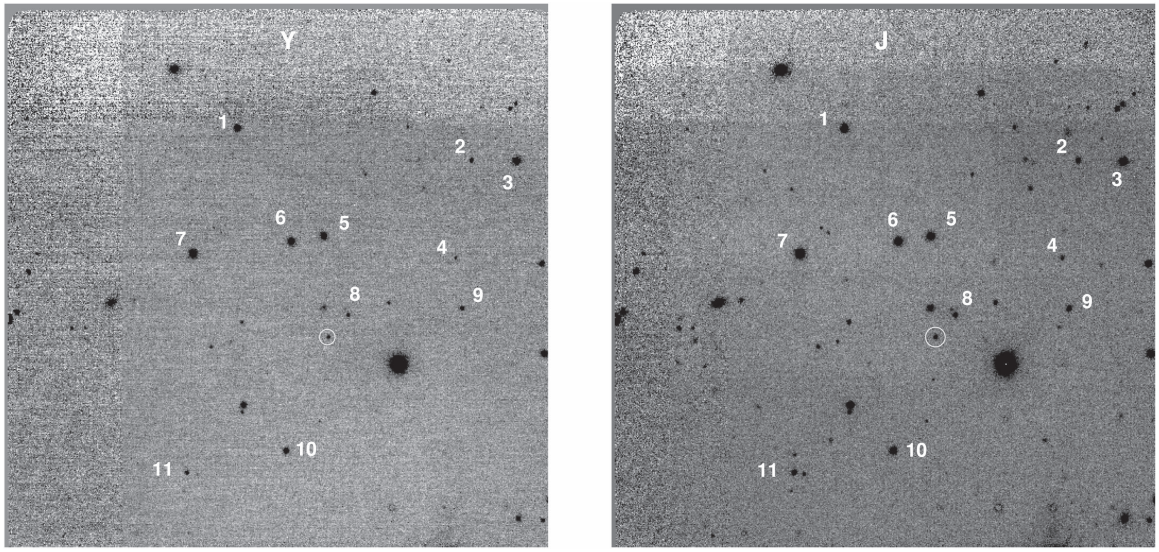

Figure 1. NIRI images of W1738 in *Y* (left) and *J* (right). The field is 2′ on a side, with north up and east to the left. W1738 is circled, and the 11 photometric comparison stars are numbered.

Table 2
Nightly Averaged *Y* and *J* for WISEP J173835.52+273258.9 and Reference Stars

Object	Nominal R.A. Decl. (hh:mm:ss.sss dd:mm:ss.s)	2013 July 17 UT			2013 August 23 UT	
		NIRI *Y* (σ)	*J* (σ)	(mag)	NIRI *Y* (σ)	*J* (σ)
W1738	17:38:35.598 27:32:58.16	19.88(0.10)	19.55(0.06)		19.94(0.14)	19.60(0.05)
star1	17:38:37.100 27:33:43.8	17.63(0.03)	17.21(0.02)		17.63(0.03)	17.28(0.04)
star2	17:38:33.249 27:33:36.90	19.52(0.07)	19.16(0.03)		19.58(0.07)	19.17(0.04)
star3	17:38:32.504 27:33:36.73	17.31(0.03)	17.07(0.02)		17.35(0.03)	17.13(0.02)
star4	17:38:33.510 27:33:15.54	20.72(0.14)	20.23(0.07)		20.74(0.15)	20.25(0.05)
star5	17:38:35.678 27:33:20.35	17.78(0.03)	17.54(0.02)		17.78(0.03)	17.58(0.03)
star6	17:38:36.211 27:33:19.11	17.59(0.04)	17.36(0.02)		17.61(0.03)	17.42(0.03)
star7[a]	17:38:37.829 27:33:16.46	16.76(0.03)	16.47(0.02)		16.77(0.02)	16.53(0.03)
star8	17:38:35.273 27:33:02.99	19.79(0.06)	19.23(0.04)		19.83(0.08)	19.25(0.04)
star9	17:38:33.401 27:33:04.49	19.38(0.04)	18.99(0.03)		19.38(0.06)	19.00(0.03)
star10	17:38:36.298 27:32:33.2	18.12(0.04)	17.66(0.02)		18.10(0.03)	17.71(0.03)
star11	17:38:37.926 27:32:28.44	19.35(0.07)	18.86(0.03)		19.37(0.06)	18.93(0.05)

Note.
[a] Star7 is 2MASS 17383786+2733160 with a Two Micron All Sky Survey (2MASS) *J* all-sky catalog magnitude of 16.598 ± 0.131.

extra care had to be taken with placement of the sky annuli. Data points that were extreme outliers, exceeding the median by 50 times the median absolute deviation, were removed. Figure 4 shows the light curves obtained. The apparently bright data points are due to hot pixels, which are caused by cosmic rays.

The average brightness of the target did not change significantly between 2013 June and October. We derive from the processed mosaics downloaded from the *Spitzer* archive [3.6] = 16.89 ± 0.08 (where the uncertainty is dominated by the uncertainty in the sky value) and [4.5] = 14.46 ± 0.01.

3. RESULTS: VARIABILITY OF W1738

Figure 4 indicates that W1738 is variable in the [4.5] bandpass with an approximately 6 hr period. We ran a simple Fourier transform analysis for each of the two [4.5] data sets, not taking into account the truncation of the time series. Figure 5 plots the result—a strong peak is found at a period of 6.0 hr for the 2013 June 30 data, and less significant peaks at 3.0 and 6.0 hr for the 2013 October 30 data set. We also ran a Lomb–Scargle periodogram analysis on both the [3.6] and [4.5] data, on the two epochs. A significant period was only found for the 2013 June 30 [4.5] data, with a broad peak in power between 5 and 7 hr.

The near-infrared light curves shown in Figures 2 and 3 suggest that W1738 may also vary at near-infrared wavelengths. In Figure 2, both *Y* and *J* brighten at around 9 and 12 hr. Trends are less clear in Figure 3, but there appears to be another 3 hr cycle present for both filters, with a minimum around 7.9 hr and maxima at 6.4 and 9.4 hr. Table 3 compares the peak-to-peak variation (range) and standard deviation of the curves obtained for W1738 and the five faint point sources (numbered 2, 4, 8, 9, and 11 in Figure 1). The stars are listed from faintest to brightest in the table. As expected, the range and standard deviation generally increase with decreasing brightness. Figures 2 and 3 show that the dispersion for W1738

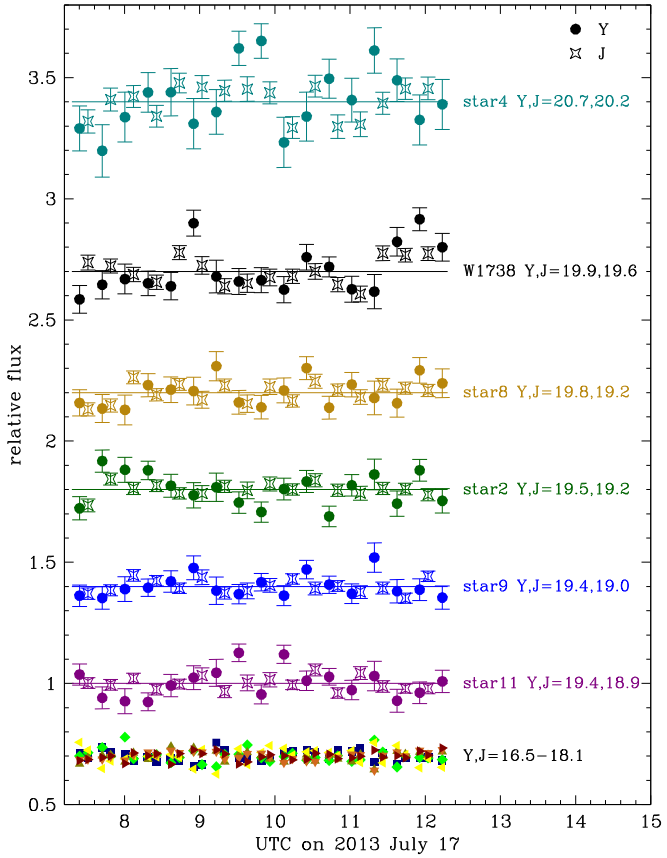

Figure 2. Light curves for W1738 and five point sources identified in Figure 1, relative to the six brighter point sources in the field, on 2013 July 17. Filled circles represent *Y* data and open stars *J* data. The errors bars are the square root of the sum of the squares of the individual measurement uncertainty and the standard deviation in the six reference measurements. The six symbols along the bottom are the light curves for the six brighter sources in the field, where each has been compared to the other five.

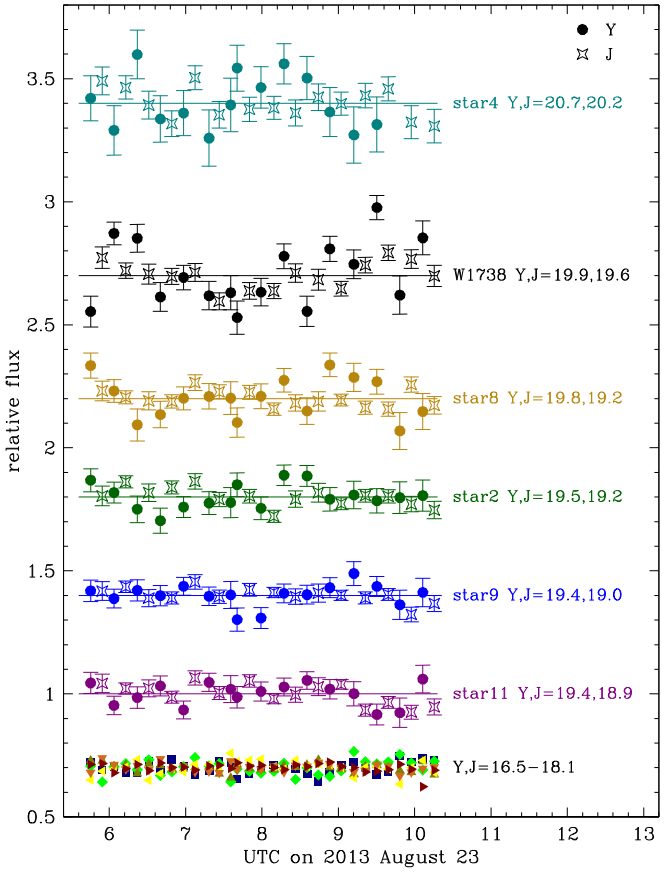

Figure 3. Same as Figure 2, but for UT 2013 August 23.

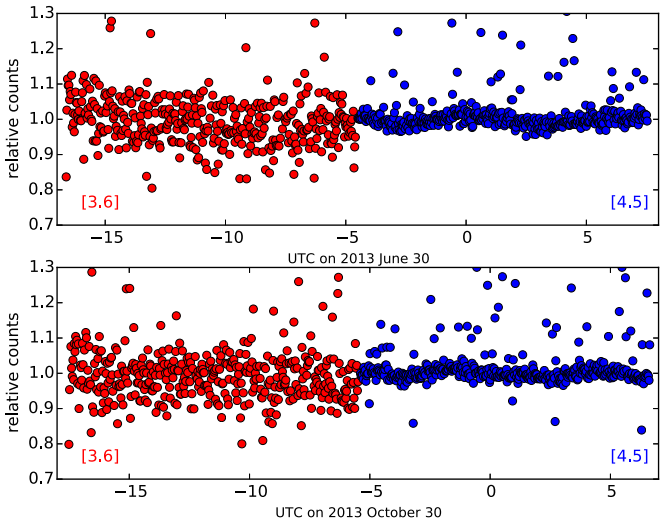

Figure 4. Relative counts obtained with IRAC on *Spitzer* using the [3.6] and [4.5] filters, as a function of time on UT 2013 June 30 and October 30. The [3.6] signal is fainter and noisier.

is similar to that of the comparison star which is fainter and larger than that of the similarly bright comparison star. The dispersion is largely driven by two or three data points, however, and the Y dwarf should be monitored for a longer period of time to confirm the presence of any variability. The standard deviation of the light curves for the five reference stars is on average 1.2× the error, while that for W1738 is 1.9× the error. The fact that the 3 hr cycle is also seen in the mid-infrared data, and that models calculate a 1 μm variability amplitude ∼10× the 4 μm variability amplitude (Section 4.2), indicates that the near-infrared variability may be real. We interpret the data as implying that W1738 is variable at 1 μm at the $\lesssim 2\sigma$ confidence level.

Based on the Fourier transform results and our visual inspection of the light curves, 3 and 6 hr cycles are present in the W1738 data. We therefore fit the [4.5] light curves assuming a double-sinusoid model, where the second sinusoid has a period half as long as the first. The amplitudes and phases of the two sinusoids can vary freely. A possible physical explanation of this double sinusoid, where the second period is half of the first, is presented in Section 4.3. The model is

$$F(t) = A_1 \sin\left(\frac{2\pi}{P}t + \phi_1\right) + A_2 \sin\left(2\frac{2\pi}{P}t + \phi_2\right) + C,$$

where A is semiamplitude in %, P is period in hours, t is time in hours, ϕ is phase in radians, and C is a constant.

The fitting procedure is described in detail in Cu16. Briefly, we assume that the uncertainties are Gaussian and account for the bad data points following Hogg et al. (2010), whereby we assume that they are generated from a normal distribution with a mean $y_{\rm bad}$ and a variance of $\sigma_{\rm bad}$. The joint posterior

distribution of the parameters A_1, A_2, ϕ_1, ϕ_2, P, C, $\sigma_{\rm good}$, and $\mathcal{P}_{\rm bad}$ (the probability that a given data point is bad) is sampled using a Markov Chain Monte Carlo (MCMC) method. Distributions for each model parameter are computed by marginalizing over the other parameters.

The one- and two-dimensional projections of the posterior probability distributions of the model parameters for the 2013 June 30 [4.5] sequence are shown in Figure 6. Figures 7 and 8 show the resulting best fits to the [4.5] data for the two epochs and the residuals between fit and data. As was also indicated by the initial Fourier transform, the data from 2013 June 30 are dominated by the longer-period sinusoid, while the 2013 October 30 data consist of two sinusoids with almost equal amplitude. A good fit could not be achieved with the noisy [3.6] data; however, extrapolating the sinusoids to earlier times shows that the [3.6] data are not inconsistent with variability at the same amplitude and phase as the [4.5] data (Figure 4). Table 4 gives semiamplitude, period, and phase for each of the two sinusoids on each epoch, using the [4.5] data only.

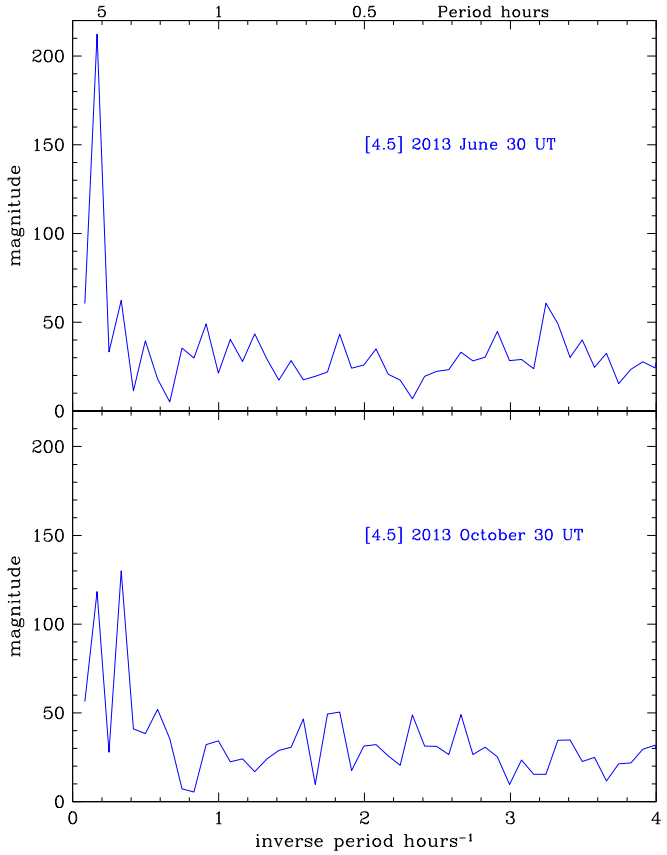

Figure 5. Results of a discrete Fourier transform analysis of the 12 hr data sets obtained with the [4.5] filter on 2013 June 30 and October 30, UT. Results are expressed as inverse period in hours, and magnitude.

4. DISCUSSION

4.1. Observed Variability in Brown Dwarfs and Giant Planets

There are no other published studies of variability at both near-infrared and mid-infrared wavelengths for Y dwarfs at the time of writing. Nine T dwarfs do have such data published, and these results are summarized in Table 5. Variability is found in five of the nine T dwarfs. Generally the periods are found to be the same at both near- and mid-infrared wavelengths, and the near-infrared amplitudes are similar to or larger than the mid-infrared amplitude (although the near- and mid-infrared data are likely to not have been taken at the same time, and amplitudes are likely to vary with time).

The variability measurements presented here for W1738 are in general agreement with results from other brown dwarf studies. Crossfield (2014) presents a multiwavelength collation of variability amplitude and period and projected rotational velocities for late-type M, L, and T dwarfs. The Crossfield sample of L and T dwarfs has variability periods of 1.5–10 hr and peak-to-peak amplitudes of 0.1%–120%, although most have amplitudes of 1%–15%. The *Spitzer* study of 39 single L3–T8 dwarfs by Metchev et al. (2015) found that 19 varied; peak-to-peak amplitudes were 0.8%–4.6% and periods were 1.6–24 hr. Recently Zhou et al. (2016) have determined a rotation period of about 11 hr for the young planetary-mass L dwarf 2MASSWJ 1207334-393254b, based on near-infrared variability with peak-to-peak amplitudes of ∼2%. In Cu16 we monitored the Y0.5(pec) W1405 with *Spitzer* and found variability with peak-to-peak amplitude of 7% and a period of 8.5 hr. Cu16 showed that the variability could be reproduced by a single bright spot model, with the light-curve period equal to the rotational period, meaning that W1405 has the longest rotation period measured to date for spectral types later than T3.

Variability seen in the surface features of the solar system gas giants is also a useful reference point for cold Y dwarfs. Gelino & Marley (2000) used observations of Jupiter to show that, were it to be unresolved, 20% variability would be observed at 4.8 μm with a period equal to the planet's rotation period of 9.9 hr. The variability in this case is predominantly due to Jupiter's Great Red Spot. Sromovsky et al. (2012) present observations of episodic bright and dark spots on Uranus. One and then two bright spots were seen on the planet's surface in 2011, drifting at very different rates, and

Table 3
Observed 1 μm Photometric Dispersion for WISEP J173835.52+273258.9 and Five Faint Reference Stars

Object	*Y*, *J* Magnitude	2013 July 17 UT						2013 August 23 UT					
		Y%			*J*%			*Y*%			*J*%		
		Range	σ	Error	Range	σ	Error	Range	σ	Error	Range	σ	Error
star4	20.7, 20.2	45.3	13.2	9.3	18.4	6.7	4.6	33.9	11.2	9.8	20.0	6.3	5.3
W1738	19.9, 19.6	33.1	10.0	5.6	17.1	5.5	3.1	44.7	13.5	5.9	19.7	5.6	3.6
star8	19.8, 19.2	18.0	5.9	5.4	13.2	3.9	2.8	26.8	8.3	5.6	10.8	3.4	3.1
star2	19.5, 19.2	22.8	6.8	4.8	10.9	2.6	2.6	18.6	5.1	5.0	14.2	3.8	3.0
star9	19.4, 19.0	16.6	4.7	4.5	9.4	2.8	2.5	18.7	4.6	4.4	13.2	3.0	2.8
star11	19.4, 18.9	20.2	6.1	4.4	9.6	2.7	2.4	14.4	4.7	4.3	13.9	4.4	2.8

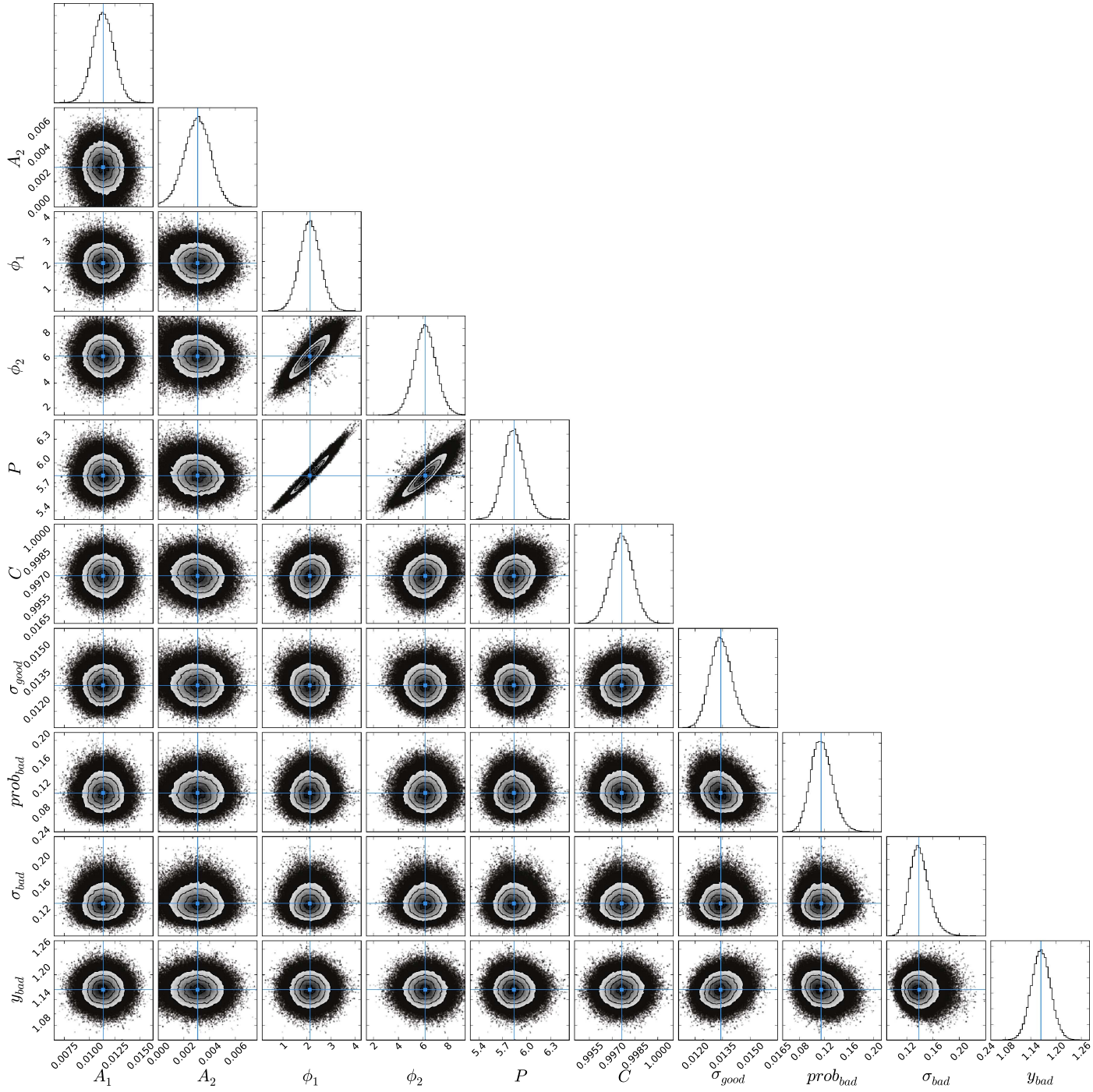

Figure 6. Probability distribution for parameters describing a double-sinusoid fit to the light curve measured on UT 2013 June 30 in the IRAC [4.5] filter.

evolving over a period of months. Simon et al. (2016) present a 49-day light curve for Neptune using *Kepler*. The data are compared to contemporaneous images taken with the Keck telescope at 1.65 μm and to *Hubble Space Telescope (HST)* visible imaging taken several months later. The authors find that a single large, long-lived storm that is seen in their Keck images dominates the *Kepler* and *HST* light curves. The periodicity of the long-term variability is consistent with the planet's rotation and surface wind speed at the latitude of the storm. The short-term variability is interpreted as being due to smaller or fainter clouds.

4.2. Models of Variability in Brown Dwarfs and Giant Planets

Three-dimensional simulations of convection in brown dwarf and giant planet interiors by Showman & Kaspi (2013) show that significant circulation is generated at both small and large scales. Large-scale horizontal temperature variations of tens of kelvin are produced, resulting in flux variations of a few percent on rotation timescales. Stratified turbulence can generate vortices and storms, and the circulation can support the formation of patchy clouds. These models produce vertical velocities consistent with the chemical mixing observed in brown dwarf atmospheres, plausible surface wind speeds, and

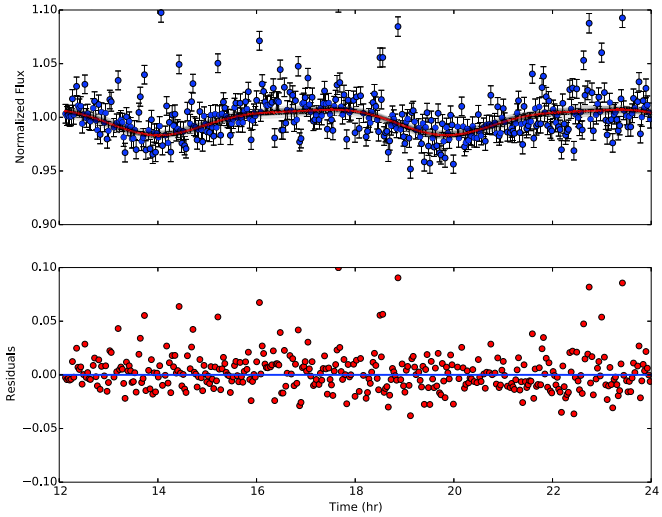

Figure 7. UT 2013 June 30 [4.5] light curve showing the best double-sinusoid model fit (red) with parameters given in Table 4 and 100 randomly selected parameter sets from the MCMC chain (gray). Residuals shown in lower panel.

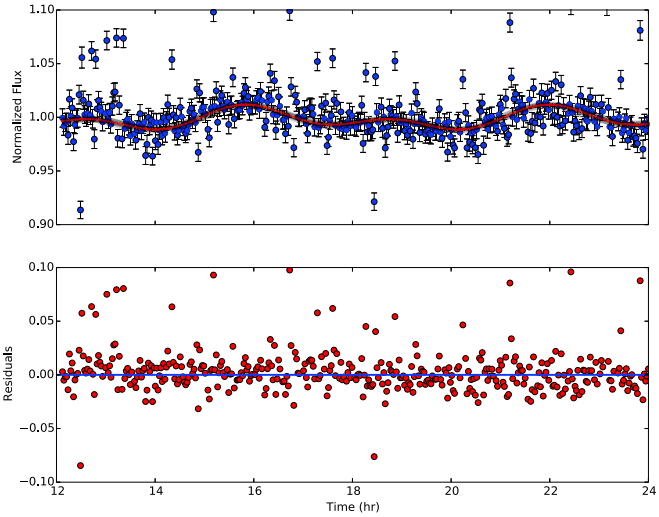

Figure 8. UT 2013 October 30 [4.5] light curve showing the best double-sinusoid model fit (red) with parameters given in Table 4 and 100 randomly selected parameter sets from the MCMC chain (gray). Residuals shown in lower panel.

timescales for the evolution of the light curve that are in agreement with observations.

It is likely that both thermal and cloud cover fluctuations are important sources of variability in giant planets and brown dwarfs (e.g., Morley et al. 2014; Robinson & Marley 2014). Although the $T_{\rm eff} \approx 400$ K atmospheres of Y dwarfs are expected to be essentially clear, Morley et al. (2012, their Figure 4) show that flux emitted from the 1 μm region originates deep enough in the atmosphere that it could be impacted by thin layers of KCl and Na_2S clouds. Morley et al. (2014) examine spectral variability that occurs if the clouds are patchy. Figure 1 of Morley et al. (2014) shows the 0.7–10 μm spectrum of a 400 K brown dwarf where one hemisphere has 30% cloud cover and the other 70%, and as a result they also differ by 5 K or >1% of the $T_{\rm eff}$. The difference in the resulting spectra, which is the inferred peak-to-peak variability, is calculated to be ~50% at 1 μm (Y), 40% at 1.2 μm (J), and 2% at 4.5 μm. We ran a similar model with a covering fraction of 45% on the eastern hemisphere and 55% on the western hemisphere, which produced peak-to-peak variability of 7% in Y, 5% in J, 0.5% in [3.6], and 0.8% in [4.5]. Thus, atmospheres with patchy clouds and small variations in surface temperature can reproduce the size of variability we observe at [4.5] and have tentatively observed at Y and J.

4.3. Interpretation of the W1738 Variability

Physical constraints on the rotation period of brown dwarfs can be helpful in determining the source of any observed variability. If the variation is caused by multiple surface features such as clouds or several discrete storms, then it can have a period smaller than the rotation period. If it is due to a single feature such as Jupiter's Great Red Spot or the single bright spot model used to reproduce the W1405 variability, then the period will be equal to the rotation period. The lower limit on the rotation period of any stable object can be estimated by assuming solid-body rotation and constraining the surface velocity to be less than the escape velocity. Adopting a radius equal to that of Jupiter's (which is approximately true for most brown dwarfs; see Burrows et al. 1997), we find that the period $P > 2.1/\sqrt{M}$ hr, where the mass of the brown dwarf is M Jupiter masses. Marley & Sengupta (2011, their Figure 2) more accurately derive a breakup velocity and show that for brown dwarfs or gas planets older than 0.1 Gyr the lower limit on rotation period is 5 hr or 1.8 hr for a 1 or a 10 $M_{\rm Jupiter}$ object, respectively. For W1738 with mass $\approx$5 $M_{\rm Jupiter}$ and age between 0.15 and 1.0 Gyr (Leggett et al. 2016), the rotational period must be greater than about 3 hr. We have found two dominant periodicities, 3 and 6 hr, in our data sets. The 3 hr component is very close to the breakup speed—which is very unlikely—suggesting that there are multiple features on the surface of the brown dwarf.

Metchev et al. (2015) found substantial power in periods approximately half of the best-fit period for 3 of the 19 variable L and T dwarfs in their sample. Studies of pre-main-sequence stars have also found photometric variability with periods separated by a factor of two (Tackett et al. 2003; Herbst 1989). The pre-main-sequence observations could be reproduced by a model where the rotation period was equal to the longer of the two periods, the star was viewed close to equator-on, and there were two similar spots, one on each hemisphere. The model showed that the shape and amplitude of the light curve evolved as the spots drifted in longitude (Herbst 1989). We attempted to fit a model with two equally bright spots to the W1738 data, where the spots are circular and have their own longitude, latitude, and size. The first epoch, where there is a dominant sinusoid, could be reasonably well reproduced by a two-spot model, but not the second epoch, where there are two sinusoids of different frequency of almost equal amplitude. We did not explore models with more than two spots.

We adopt the rotation period for W1738 to be the longer of the two periods observed, 6.0 $\pm$ 0.1 hr, and interpret the double-sinusoid variability as evidence of there being one or more large features present in its atmosphere. The features evolve over a period of months, such that in 2013 June the variability is dominated by a single spot or storm, and by 2013 October smaller features have developed, giving rise to the shorter period variability observed. This configuration of a dominant large system that is long-lived and multiple smaller surface features is similar to what was observed for Neptune by Simon et al. (2016,

Table 4
Parameters of Double-sinusoid Fits to [4.5] Light Curves

Epoch UTC 2013	Semiamplitude (%)		Period (hr)		Phase (rad)		Constant
	A_1	A_2	P_1	P_2[a]	ϕ_1	ϕ_2	C
June 30	0.011 ± 0.001	0.003 ± 0.001	5.8 ± 0.1	2.9	2.1 ± 0.4	6.2 ± 0.9	0.9977 ± 0.0007
October 30	0.0072 ± 0.0009	0.0066 ± 0.0009	6.13 ± 0.08	3.07	3.9 ± 0.3	0.7 ± 0.5	0.9984 ± 0.0006

Note.
[a] The period of the second sinusoid is forced to be half of the first in our fitting procedure; see the text. The light curve is described by

$$F(t) = A_1 \sin\left(\frac{2\pi}{P}t + \phi_1\right) + A_2 \sin\left(2\frac{2\pi}{P}t + \phi_2\right) + C,$$

where A is semiamplitude in %, P is period in hours, t is time in hours, ϕ is phase in radians, and C is a constant. The parameter and uncertainty values given in the table correspond to the 16th, 50th, and 84th percentiles of the marginalized distributions.

Table 5
T Dwarfs with Both Near- and Mid-infrared Variability Studies

Name	Spectral Type	Near-infrared		Mid-infrared		References
		Amplitude (%)	Period (hr)	Amplitude[a] (%)	Period (hr)	
SDSS J015141.69+124429.6	T1	$\leqslant$1.1[b]	⋯	<0.6	⋯	Rad14, Met15
2MASS J21392676+0220226	T1.5	8–26	7.72	~11	7.61	Ra12, Ya16
SDSSp J125453.90−012247.4	T2	$\leqslant$2.1[c]	⋯	<0.3	⋯	Ra14, Me15
SIMP J013656.5+093347.3	T2.5	6	2.4	~6	2.41	Ar09, Ra14, Ya16
2MASS J13243553+6358281[d]	T2.5	17	13.2	3	13	He15, Me15, Ya16
2MASSI J2254188+312349	T4	$\leqslant$0.8[e]	⋯	<0.5	⋯	Ra14, Me15
2MASS J22282889−4310262	T6	1.6	1.42	4.6	1.41	Ra14, Me15
2MASS J00501994−3322402	T7	10.8[f]	⋯	1.1	1.55	Wi14, Me15
Ross 458C	T8	<2.1	⋯	<1.4	⋯	Ra15, Me15

Notes. Amplitudes are peak-to-peak. References: Artigau et al. (2009); Heinze et al. (2015); Metchev et al. (2015); Radigan et al. (2012, 2014); Rajan et al. (2015); Wilson et al. (2014); Yang et al. (2016).
[a] Metchev et al. (2015) give variability amplitudes for both [3.6] and [4.5]; the larger of the two is listed in the table.
[b] Enoch et al. (2003) measured 45% variability in K_s for one epoch, but observations at other times have found the object to not vary.
[c] Goldman et al. (2008) report possible variations seen in spectra at $\lambda \sim 1.1$ and 1.6 μm.
[d] Burgasser et al. (2010) suggest that 2MASS J13243553+6358281 may be a close L dwarf and T dwarf binary.
[e] Enoch et al. (2003) measured 56% variability in K_s for one epoch, but observations at other times have found the object to not vary.
[f] Reanalysis of the Wi14 near-infrared data by Radigan (2014) determined a variability amplitude of <0.7%.

Section 4.1). We note that for W1738 the amplitude of the variability and the suggested wavelength dependence of the amplitude are well reproduced by models with patchy thin clouds (Section 4.2). The models have one hemisphere slightly more than half covered and the other slightly less than half covered with clouds. A hemisphere half covered in clouds could also be described as a hemisphere with a large spot, depending on the wavelength involved and the height of the clouds.

5. CONCLUSION

We obtained 12 hr of continuous *Spitzer* data on the Y0 brown dwarf W1738 at [3.6], followed by another 12 hr at [4.5]. Two sets of data were obtained 4 months apart, on 2013 June 30 and October 30. We also obtained interspersed Gemini Y and J data on W1738, with about 1.4 hr on-source at Y and 2.3 hr on-source at J, on two occasions separated by about 1 month, 2013 July 17 and August 23.

Fourier and Lomb–Scargle analyses of the mid-infrared [4.5] data suggested the presence of 3 and 6 hr periods in the data. We use a probabilistic method to fit double sinusoids to the [4.5] data (the near-infrared data cover a short time span, and the [3.6] data are too noisy). We constrain the second sinusoid to have half the period of the first, but we allow amplitude and phase to vary. We find that sinusoids with periods of 5.8 ± 0.1 hr and 6.13 ± 0.08 hr, and half those values, reproduce the observed [4.5] light curves on the two epochs well. The amplitudes range from 0.3% to 1.1%, leading to peak-to-peak variability of 3%. The shorter-time-span near-infrared data were inspected visually only. The data suggest that W1738 is also variable in the near-infrared, although only at the $\lesssim 2\sigma$ confidence level. If real, the implication is that this Y0 dwarf varied by 10%–30% in Y and 5%–15% in J, peak-to-peak, with a period of about 3 hr, at two epochs during 2013.

The observations are consistent with W1738, a 5 $M_{\rm Jupiter}$ $T_{\rm eff} \approx 400$ K Y-type brown dwarf being seen nearly equator-on, having a rotation period of 6.0 ± 0.1 hr, and having one or more large surface features that give rise to the variability. The features evolve over timescales of months. The observed variability at $\lambda \sim 4$ μm is likely due to thermal variations caused by atmospheric circulation, while the larger variations at $\lambda \sim 1$ μm, if real, may be due to the presence of patchy clouds of KCl and Na_2S in the lower regions of the atmosphere.

Based in part on observations obtained at the Gemini Observatory, which is operated by the Association of

Universities for Research in Astronomy, Inc., under a cooperative agreement with the NSF on behalf of the Gemini partnership: the National Science Foundation (United States), the Science and Technology Facilities Council (United Kingdom), the National Research Council (Canada), CONICYT (Chile), the Australian Research Council (Australia), Ministério da Ciência, Tecnologia e Inovação (Brazil), and Ministerio de Ciencia, Tecnología e Innovación Productiva (Argentina). Based in part on observations obtained with the *Spitzer Space Telescope*, which is operated by the Jet Propulsion Laboratory, California Institute of Technology, under a contract with NASA. S.L.'s research is supported by Gemini Observatory. D.S.'s work was supported in part by NASA grant NNH12AT89I from Astrophysics Theory.

We thank the referee for comments that greatly improved the paper.

REFERENCES

Artigau, E., Bouchard, S., Doyon, R., & Lafreniere, D. 2009, ApJ, 701, 1534
Beichman, C., Gelino, C. R., Kirkpatrick, J. D., et al. 2014, ApJ, 783, 68
Burgasser, A., Cruz, K. L., Cushing, M., et al. 2010, ApJ, 710, 1142
Burrows, A., Marley, M., Hubbard, W. B., et al. 1997, ApJ, 491, 856
Burrows, A., Sudarsky, D., & Lunine, J. I. 2003, ApJ, 596, 587
Crossfield, I. 2014, A&A, 566, A130
Cushing, M. C., Hardegree-Ullman, K. K., Trucks, J. L., et al. 2016, ApJ, 823, 152 (Cu16)
Cushing, M. C., Kirkpatrick, J. D., Gelino, C. R., et al. 2011, ApJ, 743, 50
Cushing, M. C., Kirkpatrick, J. D., Gelino, C. R., et al. 2014, AJ, 147, 113
Enoch, M. L., Brown, M. E., & Burgasser, A. J. 2003, AJ, 126, 1006
Fazio, G. G., Hora, J. L., Allen, L. E., et al. 2004, ApJS, 154, 10
Gelino, C., & Marley, M. S. 2000, in ASP Conf. Ser. 212, From Giant Planets to Cool Stars, ed. C. A. Griffith & M. S. Marley (San Francisco, CA: ASP)
Goldman, B., Cushing, M. C., Marley, M. S., et al. 2008, A&A, 487, 277
Heinze, A. N., Metchev, S., & Kellogg, K. 2015, ApJ, 801, 104
Herbst, W. 1989, AJ, 98, 2268
Hodapp, K. W., Jensen, J. B., Irwin, E. M., et al. 2003, PASP, 115, 1388
Hogg, D. W., Bovy, J., & Lang, D. 2010, arXiv:1008.4686
Kirkpatrick, J. D., Gelino, C. R., Cushing, M. C., et al. 2012, ApJ, 753, 156
Leggett, S. K., Morley, C. V., Marley, M. S., et al. 2013, ApJ, 763, 130
Leggett, S. K., Morley, C. V., Marley, M. S., & Saumon, D. 2015, ApJ, 799, 37
Leggett, S. K., Tremblin, P., Saumon, D., et al. 2016, ApJ, 824, 2
Liu, M. C., Dupuy, T. J., Bowler, B. P., Leggett, S. K., & Best, W. M. J. 2012, ApJ, 758, 57
Luhman, K. L. 2014, ApJL, 786, L18
Luhman, K. L., Burgasser, A. J., & Bochanski, J. J. 2011, ApJL, 730, L9
Marley, M. S., & Sengupta, S. 2011, MNRAS, 417, 2874
Metchev, S. A., Heinze, A., Apai, D., et al. 2015, ApJ, 799, 154
Morley, C. V., Fortney, J. J., Marley, M. S., et al. 2012, ApJ, 756, 172
Morley, C. V., Marley, M. S., Fortney, J. J., et al. 2014, ApJ, 787, 78
Pinfield, D. J., Gromadzki, M., Leggett, S. K., et al. 2014, MNRAS, 444, 1931
Radigan, J. 2014, ApJ, 797, 120
Radigan, J., Jayawardhana, R., Lafreniere, D., et al. 2012, ApJ, 750, 105
Radigan, J., Lafreniere, D., Jayawardhana, R., & Artigau, E. 2014, ApJ, 793, 75
Rajan, A., Patience, J., Wilson, P. A., et al. 2015, MNRAS, 448, 3775
Robinson, T. D., & Marley, M. S. 2014, ApJ, 785, 158
Saumon, D., & Marley, M. S. 2008, ApJ, 689, 1327
Schneider, A. C., Cushing, M. C., Kirkpatrick, J. D., et al. 2015, ApJ, 804, 92
Showman, A. P., & Kaspi, Y. 2013, ApJ, 776, 85
Simon, A. A., Rowe, J. F., Gaulme, P., et al. 2016, ApJ, 817, 162
Sromovsky, L. A., Hammel, H. B., de Pater, I., et al. 2012, Icar, 220, 6
Tackett, S., Herbst, W., & Williams, E. 2003, AJ, 126, 348
Tinney, C. G., Faherty, J. K., Kirkpatrick, J. D., et al. 2012, ApJ, 759, 60
Tremblin, P., Amundsen, D. S., Mourier, P., et al. 2015, ApJL, 804, L17
Wilson, P. A., Rajan, A., & Patience, J. 2014, A&A, 566, A111
Yang, H., Apai, D., Marley, M. S., et al. 2016, ApJ, 826, 8
Zhou, Y., Apai, D., Schneider, G. H., Marley, M. S., & Showman, A. P. 2016, ApJ, 818, 176